STRUCTURAL BIOLOGY

DELTEX2 C-terminal domain recognizes and recruits ADP-ribosylated proteins for ubiquitination

Syed Feroj Ahmed[1]*, Lori Buetow[1]*, Mads Gabrielsen[1], Sergio Lilla[1], Chatrin Chatrin[1,2], Gary J. Sibbet[1], Sara Zanivan[1,2], Danny T. Huang[1,2†]

Cross-talk between ubiquitination and ADP-ribosylation regulates spatiotemporal recruitment of key players in many signaling pathways. The DELTEX family ubiquitin ligases (DTX1 to DTX4 and DTX3L) are characterized by a RING domain followed by a C-terminal domain (DTC) of hitherto unknown function. Here, we use two label-free mass spectrometry techniques to investigate the interactome and ubiquitinated substrates of human DTX2 and identify a large proportion of proteins associated with the DNA damage repair pathway. We show that DTX2-catalyzed ubiquitination of these interacting proteins requires PARP1/2-mediated ADP-ribosylation and depends on the DTC domain. Using a combination of structural, biochemical, and cell-based techniques, we show that the DTX2 DTC domain harbors an ADP-ribose–binding pocket and recruits poly-ADP-ribose (PAR)–modified proteins for ubiquitination. This PAR-binding property of DTC domain is conserved across the DELTEX family E3s. These findings uncover a new ADP-ribose–binding domain that facilitates PAR-dependent ubiquitination.

INTRODUCTION

Posttranslational modifications (PTMs) dynamically regulate protein function in all known cellular processes, including DNA damage repair (DDR), apoptosis, and proteasomal degradation. Ubiquitination is a PTM in which the small 8.6-kDa protein ubiquitin (Ub) is covalently linked to a protein substrate to modulate protein localization and function (*1*). Substrate ubiquitination is performed by the consecutive action of three enzymes. Initially, Ub-activating enzyme (E1) uses Mg^{2+}-ATP (adenosine triphosphate) to activate and transfer Ub to a Ub-conjugating enzyme (E2), forming an E2~Ub thioester in which the C-terminal Gly of Ub is conjugated to the active-site Cys of the E2. In the final step, a Ub ligase (E3) catalyzes transfer of Ub from E2~Ub to a lysine on substrate, forming an amide between the lysine Nζ and the C-terminal Gly of Ub (*2*). The largest class of E3s, the RING E3s, is characterized by the presence of a RING domain that recruits E2~Ub and transfers Ub directly to substrate (*3*, *4*).

In mammals, the DELTEX (DTX) family of RING E3s comprises five members (DTX1, DTX2, DTX3, DTX3L, and DTX4) (*5*, *6*). Functionally, all members of the DTX family are mainly linked to developmental processes involving Notch signaling (*5*, *7*–*9*). In addition, DTX3L has also been shown to play a role in modifying histones during DDR (*6*, *10*, *11*). Members of the DTX family are characterized by the presence of two homologous domains at their C termini, a RING domain for Ub transfer followed by a Deltex C-terminal (DTC) domain for which the function remains unknown (*12*). The N termini of DTX family members diverge, but in DTX1, DTX2, and DTX4, this region comprises two consecutive WWE motifs (*13*). WWE motifs commonly function in binding poly–adenosine diphosphate (ADP)–ribosylated (PARylated) targets via their ability to recognize *iso*-ADP-ribose (*iso*-ADPr), the minimal subunit of PAR polymer containing the characteristic glycosidic linkage, and this has been validated for DTX1 (*14*–*16*). However, in the *Drosophila melanogaster* Dtx homolog, these two motifs comprise a single domain that binds the intracellular domain of the Notch receptor to modulate Notch signaling (*9*, *13*, *17*).

PARylated proteins are abundant at DNA lesion sites where they are critical for regulating processes such as DDR and apoptosis (*18*, *19*). In mammals, protein PARylation is performed by PAR polymerases (PARPs) (*20*). During DDR, upon detecting DNA lesions, PARP1 becomes active and promotes the formation of PAR chains on a number of targets including DTX2 (*21*, *22*). Presumably, this functions as a signal to recruit DTX2 to DNA damage sites where it then ubiquitinates its targets. However, how DTX2 recruits substrate for ubiquitination is unknown. We suspected that the DTC domain might have a role in substrate ubiquitination based on sequence contiguity with the RING domain, so we determined the structure of a C-terminal fragment of human DTX2 comprising these two domains. We subsequently identified putative DTX2 substrates using two different label-free quantitative mass spectrometry (MS) methods and validated two of the identified targets in cell-based assays. Using a combination of structural studies, cell and biochemical assays, we show that DTX2-mediated ubiquitination depends on the ability to bind PARylated substrate via the DTC domain.

RESULTS

DTX2 RING-DTC structure

To investigate a possible role for the DTC domain of the DTX family of E3 ligases in ubiquitination, we determined structures of a C-terminal fragment of human DTX2 encompassing the RING and DTC domains (residues 390–C; hereby referred to as 2RD) (Fig. 1, A and B, and Table 1). Crystals were obtained in two conditions and have either one or two molecules per asymmetric unit. On the basis of these structures, 2RD is a monomer. The RING and DTC domains of 2RD resemble the previously determined nuclear magnetic resonance structure of mouse DTX2 RING domain and crystal structure of the DTC domain from human DTX3L. Superposition of the RING (residues 390 to 479 in 2RD) or the DTC (residues 480–C in 2RD) domains yields a root mean square deviation (RMSD) ranging from 0.68 to 0.74 Å across 74 to 81 Cα atoms or an RMSD ranging from 0.50 to 0.67 Å across 97 to 106 Cα atoms. The orientation

[1]Cancer Research UK Beatson Institute, Garscube Estate, Switchback Road, Glasgow G61 1BD, UK. [2]Institute of Cancer Sciences, University of Glasgow, Glasgow G61 1QH, UK.
*These authors contributed equally to this work.
†Corresponding author. Email: d.huang@beatson.gla.ac.uk

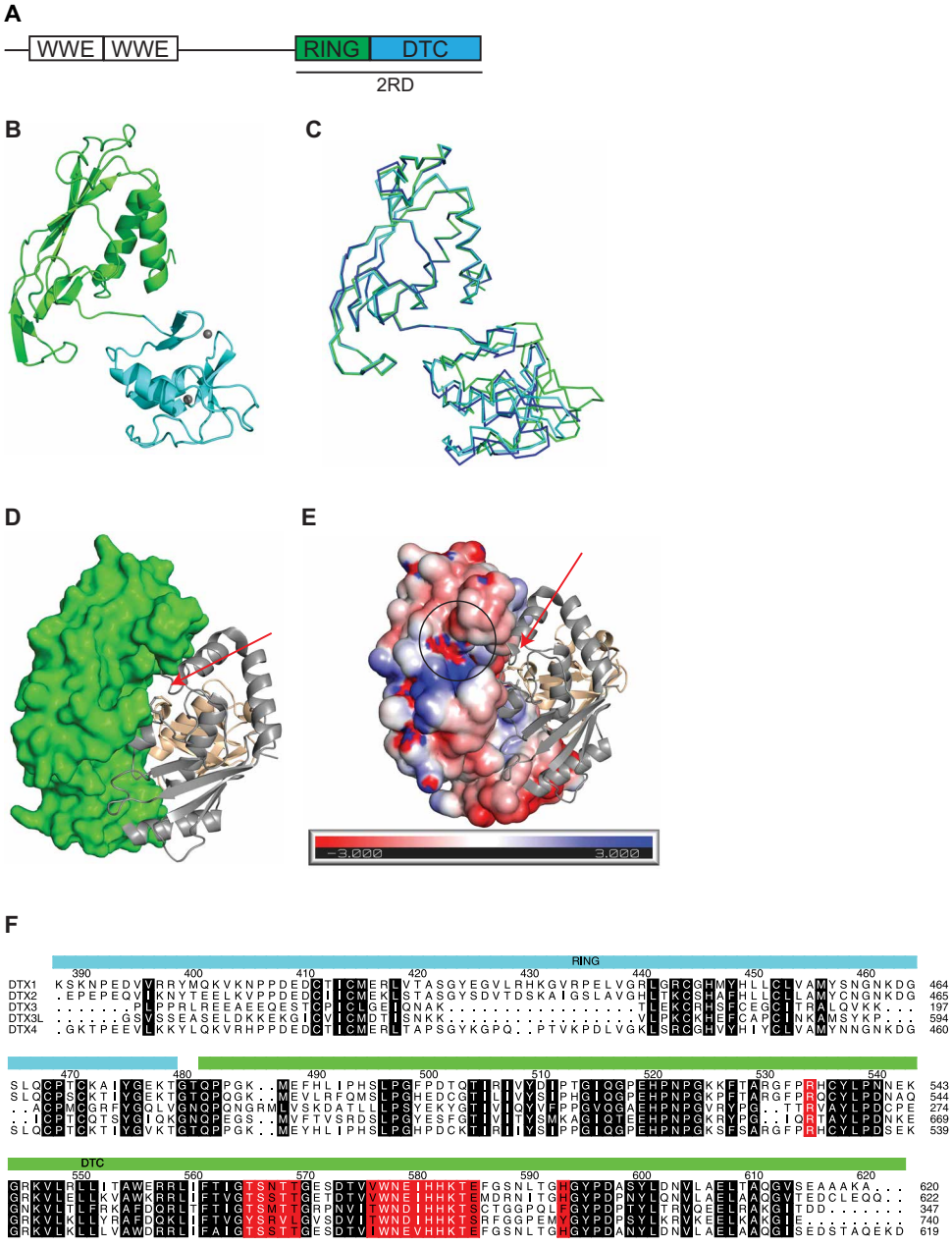

Fig. 1. Structure of 2RD. (**A**) Domain architecture of DTX2. (**B**) Cartoon representation of 2RD from crystal condition 1. The RING and DTC domains are colored cyan and green, respectively. Zn^{2+} ions are shown as gray spheres. (**C**) Cα ribbon overlay of the three molecules of forms 1 and 2 of 2RD. The DTC domains have been superposed to illustrate the flexibility between the RING and DTC domains. The molecule from condition 1 is colored green, and the two molecules from condition 2 are colored cyan and blue. (**D**) Model of 2RD bound to UbcH5B~Ub. The RING domain of 2RD was superposed with the RNF38 RING domain from the RNF38-UbcH5B~Ub complex (PDB 4V3L) to generate the model. Surface representation of 2RD colored green and oriented as in (A); cartoon representation of UbcH5B~Ub with UbcH5B and Ub colored gray and wheat, respectively. The red arrow indicates the position of the UbcH5B~Ub thioester. (**E**) Model of 2RD bound to UbcH5B~Ub. As in (D) but with surface representation of 2RD colored by charge potential. The circled area contains the charged pocket proximal to the UbcH5B~Ub thioester (indicated by the red arrow). (**F**) Sequence alignment of the RING-DTC fragment from the DTX family of E3s. Residues comprising the charged pocket proximal to the modeled UbcH5B~Ub thioester are highlighted in red, and conserved residues defined by an ALSCRIPT (*56*) level of 0.7 are highlighted in black.

between the RING and DTC domains differs across the three molecules in the 2RD crystal structures, suggesting that there is a degree of rotational flexibility between the two domains (Fig. 1C). The three molecules of 2RD superpose with an RMSD ranging from 0.98 to 2.69 Å across 195 to 213 Cα atoms, whereas the RING domains superpose with an RMSD ranging from 0.36 to 0.47 Å and the DTC domains superpose with an RMSD ranging from 0.30 to 0.31 Å across 72 to 80 and 120 to 125 Cα atoms, respectively.

The proximity of the RING and DTC domains and the rotational flexibility between them suggest that the DTC domain may have a role in substrate ubiquitination. To further explore this possibility, we built a model of 2RD bound to UbcH5B~Ub by superposing the

Table 1. Data collection and refinement statistics.

	DTX2 form 1	DTX2 form 2	DTX2-ADPr
PDB code	6Y22	6Y2X	6Y3J
Data collection			
Space group	$P3_221$	$C222_1$	$P3_221$
Cell dimensions			
a, *b*, *c* (Å)	106.42, 106.42, 74.67	41.76, 219.58, 120.85	104.93, 104.93, 74.54
α, β, γ (°)	90.0, 90.0, 120.0	90.0, 90.0, 90.0	90.0, 90.0, 120.0
Resolution (Å)	92.16–2.07	60.43–1.77	90.95–2.60
	(2.12–2.07)*	(1.82–1.77)	(2.72–2.60)
R_{merge}	7.6 (74.8)	5.2 (77.0)	27.4 (161)
R_{pim}	3.7 (36.0)	3.2 (47.4)	9.9 (59.7)
$I/\sigma I$	16.5 (3.3)	14.4 (1.8)	5.3 (1.0)
CC(1/2)	0.999 (0.973)	0.999 (0.581)	0.994 (0.822)
Completeness (%)	99.7 (97.3)	100.0 (100.0)	100.0 (100.0)
Redundancy	10.0 (10.0)	6.6 (6.8)	9.3 (8.9)
Refinement			
Resolution (Å)	29.01–2.07 (2.12–2.07)	60.43–1.77 (1.82–1.77)	45.48–2.6 (2.72–2.60)
No. of reflections	29,929	54,018	28,029
R_{work}/R_{free} (%)	18.02/20.92	24.2/27.4	23.76/28.22
No. of atoms			
Protein	1,742	2,998	1,745
Ions	2	4	2
Ligand			36
Water	92	258	20
B-factors (Å^2)			
Protein	56.3	56.44	58.35
Ions	48.17	73.50	61.96
Ligand			56.71
Water	55.15	51.78	49.41
RMSD			
Bond lengths (Å)	0.006	0.006	0.011
Bond angles (°)	0.829	0.841	1.331

*Values in parentheses are for highest-resolution shell.

RING domain of 2RD onto the RING domain of the E3 RNF38 bound to UbcH5B~Ub [Protein Data Bank (PDB) 4V3L] (Fig. 1D). In the model, UbcH5B~Ub abuts the DTC domain and the thioester is oriented toward a charged pocket on the DTC domain (Fig. 1E). This pocket comprises residues that are highly conserved in sequence alignment of the RING-DTC domains of DTX family members (Fig. 1F) and in structural alignment with the DTX3L DTC domain. On the basis of the apparent proximity of the thioester to this conserved pocket and the flexibility between the RING and DTC domains, we thought that the DTC domain might bind substrate during DTX2-mediated ubiquitination (Fig. 1D). Furthermore, because this pocket is conserved in all DTX family members, it suggests that DTC interactors might share a common binding motif (Fig. 1, E and F).

DTX2 interacts primarily with DDR proteins

Little is known about the interactome of DTX2, so to identify potential binding partners of DTX2, we performed MS-based proteomics on Myc-trap immunoprecipitations (IPs) from whole-cell lysates of human embryonic kidney (HEK) 293 cells transiently expressing Myc-tagged DTX2 (Myc-DTX2) or empty vector (EV). We identified 13 potential binding partners in total and found that 10 of these are active in DDR (Fig. 2A and data S1). Among these, PARP1 was one of the highest scoring binding partners identified. We validated DTX2 interactions in coimmunoprecipitations with the following subset of binding partners identified in the pull-down: PARP1, FACT complex subunits SPT16 and SSRP1, x-ray repair cross-complementing proteins 5 and 6 (XRCC5 and XRCC6), and replication protein A 70-kDa DNA binding subunit (RPA1) (Fig. 2B).

To identify which of the DTX2-interacting substrates are ubiquitinated by DTX2, we next performed Ub remnant profiling on whole-cell lysates from HEK293 cells overexpressing green fluorescent protein (GFP)–DTX2 or GFP. Because PARP1 and other DDR proteins were abundant in the pull-down, we thought that DTX2 might have a role in DDR and performed the experiments following the induction of DNA damage with H_2O_2. Eight of the proteins identified in the Myc-trap pull-down were also present in the Ub remnant assay, including SPT16 and PARP1. In addition, 263 of the 2087 peptides (corresponding to 71 of 1035 proteins) that were ubiquitinated in cells overexpressing GFP-DTX2 are involved in DDR (Fig. 2C and data S2). Despite their importance in DDR (*23*), no histones were identified with the Myc-trap pull-down and only one, namely, histone H3.1, was found in the Ub remnant assay. We confirmed the interaction of DTX2 with histone H3.1 by coimmunoprecipitation (fig. S1) and then validated that both histone H3.1 and SPT16 were ubiquitinated in HEK293 cells by DTX2 (Fig. 2D).

Because PARP1 was identified in the DTX2 interactome and PARylation is a common posttranslational feature of many identified binding partners of DTX2 including SPT16 and histone H3.1 as well as DTX2 itself (*21*, *24*), we next investigated the effects of ABT-888 (veliparib), a PARP1 and PARP2 inhibitor, on substrate binding and ubiquitination. In the presence of ABT-888, none of the selected binding partners from the Myc-trap pull-down coimmunoprecipitated with DTX2 (Fig. 2B) nor did histone H3.1 (fig. S1). In addition, when cells were treated with ABT-888, ubiquitination of histone H3.1 and SPT16 in the presence of ectopically expressed DTX2 was reduced to a level similar to the control EV (Fig. 2D). Basal histone H3.1 and SPT16 mono-ubiquitination were observed in the control EV, likely because of other E3s or endogenous DTX2. In in vitro assays, glutathione *S*-transferase (GST)–2RD autoubiquitination was unaffected by ABT-888 (Fig. 2E), excluding the possibility that ABT-888 interferes directly with Ub transfer by the RING domain. Together, these data demonstrate that there is a link between ubiquitination by DTX2 and PARylation by PARP1.

Ubiquitination of PARylated substrates requires DTC domain

WWE domains commonly bind PAR polymer (*16*), and in the RING E3 ligase RNF146, this domain links substrate PARylation and ubiquitination (*16*, *25*–*27*); hence, there was a possibility that

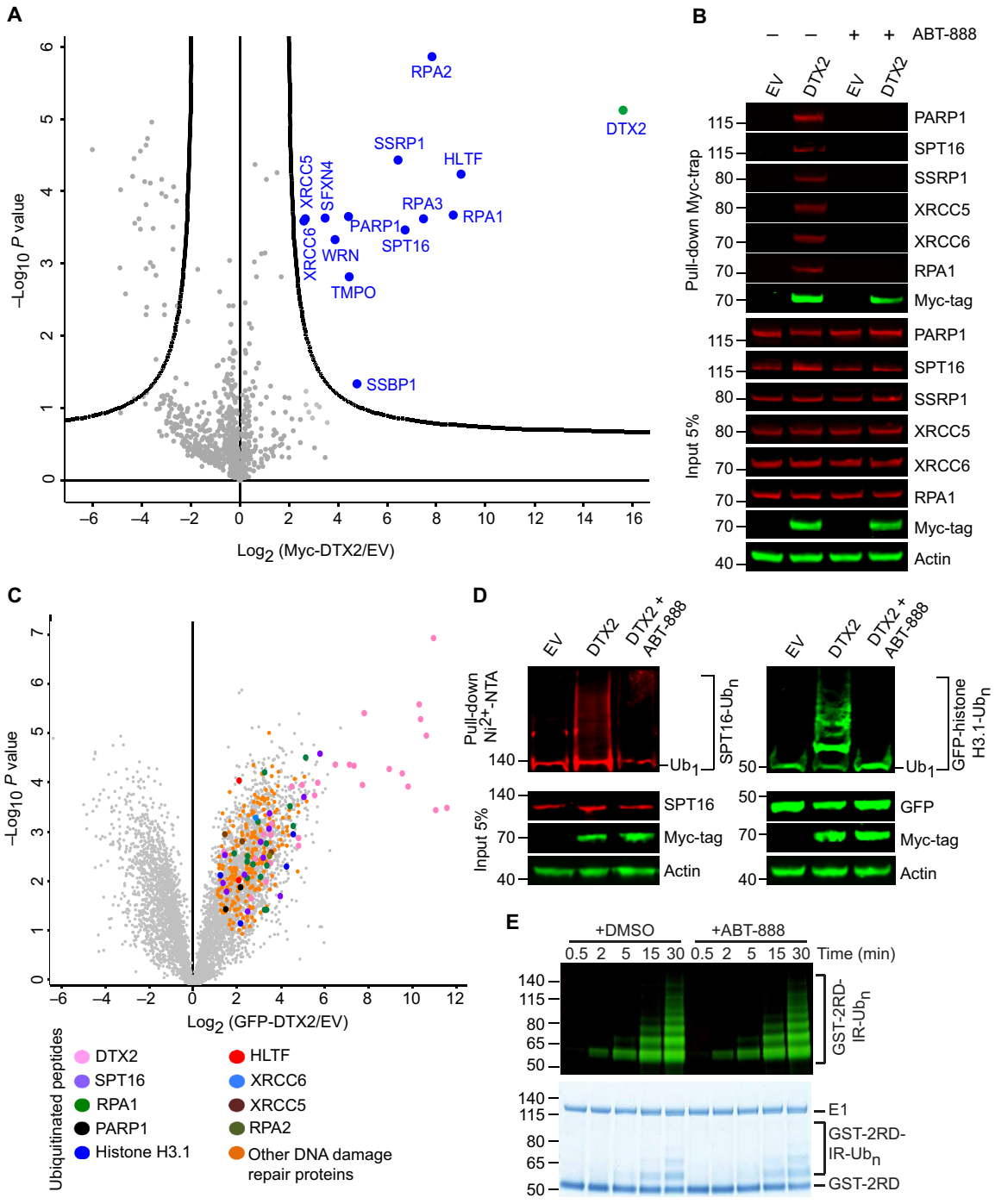

Fig. 2. Identification of DTX2 substrates. (**A**) Volcano plot displaying proteins that bind to Myc-DTX2 versus EV. Myc-trap pull-downs were performed in triplicate on whole-cell lysates from HEK293 cells expressing Myc-DTX2 or EV. Proteins shown as blue dots were identified as significantly enriched proteins using a *t* test with a 5% false discovery rate (FDR) in all three replicates and more abundant in Myc-DTX2 pull-downs compared to EV. Associated with data S1. (**B**) Immunoblots of Myc-trap pull-downs of whole-cell lysates from HEK293 cells expressing Myc-DTX2 or EV in the presence and absence of ABT-888 using anti-PARP1, anti-SPT16, anti-SSRP1, anti-XRCC5, anti-XRCC6, anti-RPA1, anti–Myc-tag, or anti-actin as indicated. (**C**) Volcano plot displaying $\log_2$ fold change in intensities in peptides modified with Ub from lysates from HEK293 cells expressing GFP-DTX2 compared to EV. Assays were performed in triplicate, and significant changes in ubiquitinated peptide intensities were determined using a Student's *t* test with a 1% FDR (permutation-based). Significantly changed ubiquitinated peptides present in all three replicates, more abundant in lysates from cells expressing GFP-DTX2, and from proteins annotated in the Gene Ontology database with the term "DNA repair" are colored as indicated. Associated with data S2. (**D**) Immunoblots of SPT16 (left) and histone H3.1 (right) ubiquitination by DTX2 in HEK293 cells expressing His-Ub, EV or Myc-DTX2, and GFP–histone H3.1 (right only) in the presence and absence of ABT-888. The cell lysates and Ni^{2+}–pull-down products were immunoblotted with anti-GFP, anti-SPT16, anti–Myc-tag, or anti-actin antibodies as indicated. (**E**) Reduced in vitro autoubiquitination assay showing the formation of GST-2RD-IR-Ub_n over time in the presence and absence of ABT-888. IR-Ub, Ub labeled with near-infrared dye. Visualized with the Odyssey CLx Imaging System (LI-COR Biosciences, top) and subsequently by staining with InstantBlue (Expedeon, bottom).

the tandem WWE domains in DTX2 could play a similar role in binding PARylated substrate and facilitating ubiquitination. Given that the WWE domains of DTX2 are uncharacterized, we initially performed in vitro pull-down assays with a fragment comprising the N-terminal tandem WWE domains of DTX2 (DTX2-WWE) and found that this fragment bound PARylated PARP1 but not PARP1 (fig. S2, A and B). Furthermore, when tested in mammalian cell lysates, this fragment was sufficient to pull down histone H3.1 and SPT16 (Fig. 3A) but not in the presence of ABT-888. Functional assays and sequence alignment with the WWE domain of RNF146 have implicated Trp^{24} and Trp^{114} as critical PAR-binding residues in DTX2 (*16*), so we generated a W24A W114A double mutant (WDM) and tested its ability to bind PARylated substrates in mammalian cell lysates. DTX2-WWE WDM did not bind histone H3.1 or SPT16 (Fig. 3A). Together, these data show that the tandem WWE domains of DTX2 bind PARylated substrate.

To explore the possibility that the tandem WWE domains in DTX2 serve as the functional link for binding PARylated substrate for ubiquitination, we performed cell-based ubiquitination assays on histone H3.1 and SPT16 using full-length DTX2 wild-type (DTX2 WT) and DTX2-W24A W114A (DTX2 WDM). Unexpectedly, both targets were ubiquitinated with similar efficiency (Fig. 3B) in the presence of DTX2 WT or DTX2 WDM, suggesting that the WWE domains have a limited or nonessential role in DTX2-mediated substrate ubiquitination. Involvement of the tandem WWE domains in substrate ubiquitination by DTX2 cannot be excluded given their PAR-binding potency. However, on the basis of the lack of sequence contiguity of the WWE and RING domains, we speculated that the contribution of the tandem WWE domains on DTX2 substrate ubiquitination might not be direct. Hence, we investigated the DTC domain as a possible link between substrate PARylation and ubiquitination based on our earlier structural analysis (Fig. 1). We tested the RING-DTC fragment of DTX2 in cell-based ubiquitination assays and found that it was sufficient to mediate ubiquitination of histone H3.1 and SPT16 (Fig. 3C); furthermore, ABT-888 reduced substrate ubiquitination by this DTX2 fragment to a level similar to that of the EV (Fig. 3C). From these data, we surmised that the DTC domain plays a role in linking PARP1-mediated PARylation and substrate ubiquitination.

Whether substrate ubiquitination depends on PARylation of DTX2 itself or a DTX2-binding partner is unclear. To investigate, we performed in vitro PARylation assays on histone H3.1 and 2RD with PARP1. Histone H3.1 was only PARylated in the absence of ABT-888, whereas 2RD was not PARylated in either condition (Fig. 3D). We then attempted to probe whether only PARylated histone H3.1 was ubiquitinated by 2RD in vitro but could not because this form of the histone was insoluble. Instead, we produced a GFP-tagged histone H3.1 fragment (H3.1 tail-GFP; fig. S2C) that encompasses the identified ubiquitination site (data S2) and treated it with PARP1 and biotinylated nicotinamide adenine dinucleotide (NAD^+) to generate PARylated H3.1 tail-GFP for in vitro ubiquitination assays with 2RD. PARylated H3.1 tail-GFP was ubiquitinated by 2RD but not unmodified H3.1 tail-GFP (Fig. 3E). To further verify the dependency on substrate PARylation for 2RD-mediated ubiquitination, we also tested PARP from the bacterium *Herpetosiphon aurantiacus* (HaPARP) as a model substrate. His-tagged HaPARP was treated with biotinylated NAD^+ to generate auto-PARylated HaPARP and pulled down with Ni^{2+}-NTA (nitrilotriacetic acid) following ubiquitination with 2RD in the presence of E1, UbcH5B, and Ub. In the presence of 2RD, the apparent molecular weight of the bulk of the PARylated HaPARP shifted upward, consistent with ubiquitinated PARylated HaPARP. In addition, a higher molecular weight smear containing Ub and HaPARP was enhanced when HaPARP was PARylated (Fig. 3F). A basal smear of ubiquitinated products was observed in the control reaction lacking HaPARP, which was likely due to nonspecific binding to Ni^{2+}-NTA (Fig. 3F). These results demonstrate that substrate PARylation is the mediating factor between these two PTMs. The proximity of the RING and DTC domains and PARylation-dependent ubiquitination requirements suggest that the DTX2 DTC domain plays a role in directly recruiting PARylated substrates.

ADPr binding site on DTX2 RING-DTC

To probe the mechanism of PAR binding by the DTC, we determined the structure of 2RD bound to ADPr to 2.60 Å (Fig. 4A and Table 1). The structure most closely resembles the apo-structure from condition 1, having an RMSD of 0.39 Å across 208 Cα atoms. ADPr binds within the pocket identified as a putative substrate-binding site in our model of apo-2RD bound to UbcH5B~Ub (Fig. 1) and makes numerous hydrophobic and electrostatic interactions with residues in the DTC domain (Fig. 4, B and C). Notably, most of the ADPr-interacting residues from the DTC are conserved across the DTX family (Fig. 1F): Trp^{578} and His^{594} form π bonds with the adenine ring of ADPr, and His^{582} forms a hydrogen bond with the C2′ hydroxyl of the ribose proximal to the adenine ring. The side chain of Arg^{535} and main chain of Ser^{567} and Ser^{568} form putative hydrogen bonds with oxygen atoms in the diphosphate motif of ADPr, and the side chains of Arg^{535} and Trp^{578} form weak electrostatic interactions with the ribose distal to the adenine ring.

To validate our complex structure and substrate ubiquitination model, we generated two mutants of DTX2 and assessed their ability to ubiquitinate our model substrate PARylated HaPARP in vitro and histone H3.1 and SPT16 in cells. RING domain residues Ile^{414} and Tyr^{425} were substituted with Ala to abrogate E2~Ub binding in one mutant [referred to as RDM (RING double mutant)], and DTC domain residues Ser^{568}, His^{582}, and His^{594} were substituted with Ala to abolish ADPr binding in the second [referred to as DTM (DTC domain triple mutant)]. Surface plasmon resonance (SPR) binding assays confirmed that GST-2RD RDM did not bind UbcH5B S22R (a variant lacking the noncovalent "backside" Ub interaction) or UbcH5B S22R C85K–Ub (a stably conjugated variant of UbcH5B~Ub), whereas GST-2RD and GST-2RD DTM displayed similar binding affinities for UbcH5B S22R and UbcH5B S22R C85K–Ub (fig. S3 and table S1). Correspondingly, in Ub transfer assays, the fraction of UbcH5B~Ub discharged to lysine by 2RD and 2RD DTM was comparable, whereas the fraction discharged by 2RD RDM was approximately the same as in the absence of E3 (Fig. 4, D and E). These data established that the RING domain of the DTC mutant, 2RD DTM, binds UbcH5B~Ub and is catalytically competent. Next, we performed in vitro ubiquitination of PARylated HaPARP by monitoring shifts in the PARylated HaPARP bands as the readout of ubiquitination and observed that neither GST-2RD RDM nor DTM promoted ubiquitination of PARylated HaPARP (Fig. 4F). Likewise, in cells, ubiquitination of histone H3.1 or SPT16 by Myc-DTX2 RDM or DTM was similar to Myc-DTX2 WT treated with ABT-888 (Fig. 4G). These data are consistent with our proposed model in which the DTC domain binds PARylated substrates to facilitate ubiquitination by the RING domain.

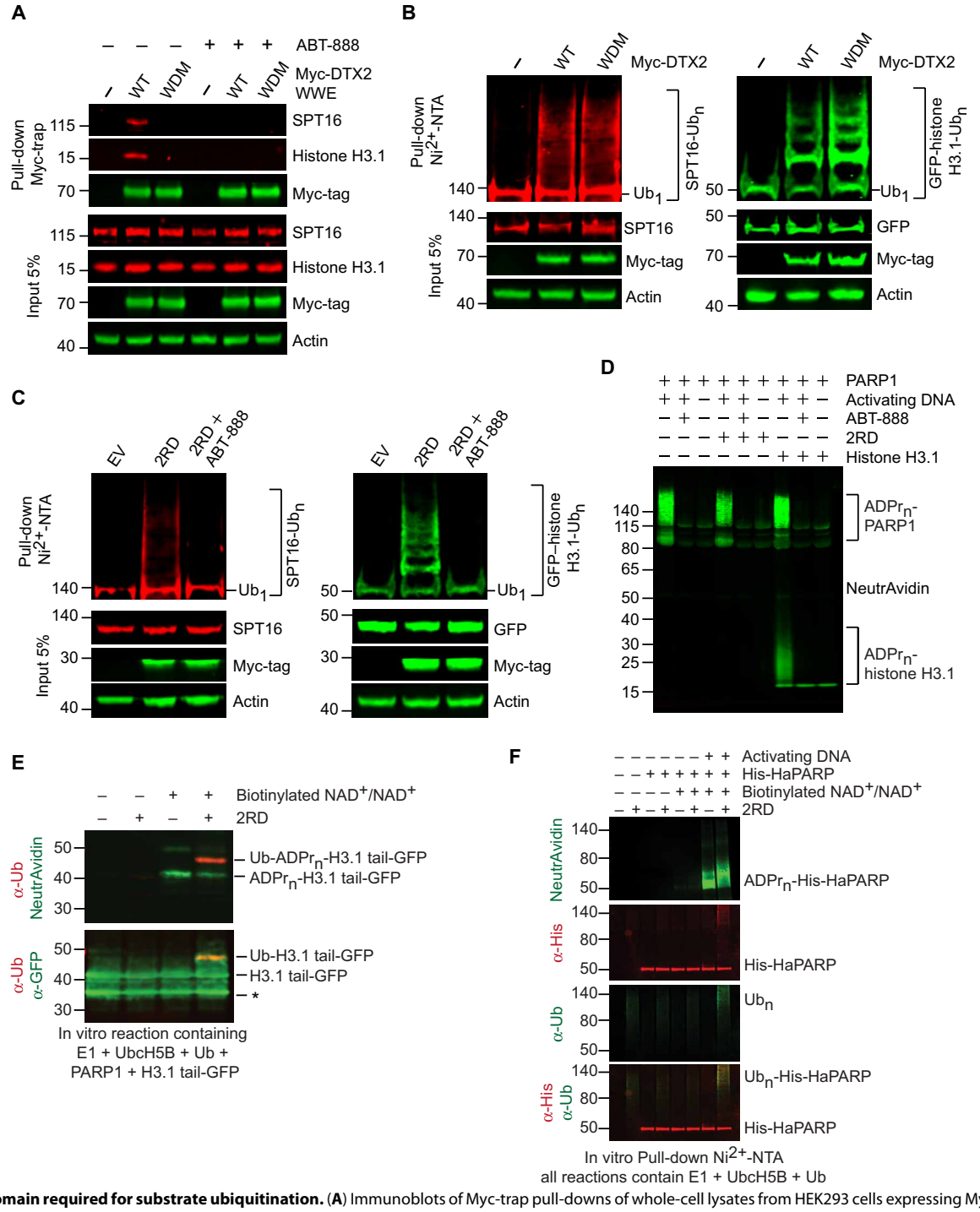

Fig. 3. DTC domain required for substrate ubiquitination. (**A**) Immunoblots of Myc-trap pull-downs of whole-cell lysates from HEK293 cells expressing Myc-DTX2 WWE variants or EV (–) in the presence and absence of ABT-888 using anti-SPT16, anti–histone H3.1, anti–Myc-tag, or anti-actin as indicated. (**B**) Immunoblots of SPT16 (left) and histone H3.1 (right) ubiquitination by DTX2 in HEK293 cells expressing His-Ub, GFP–histone H3.1 (right only), and EV (–) or full-length Myc-DTX2 variants: WT (wild type) or WDM (WWE domain mutant); cell lysates and Ni^{2+}–pull-down products were immunoblotted with anti-GFP, anti-SPT16, anti–Myc-tag, or anti-actin antibodies as indicated. (**C**) Immunoblots of SPT16 (left) and histone H3.1 (right) ubiquitination by 2RD in the presence and absence of ABT-888 in HEK293 cells expressing His-Ub, GFP–histone H3.1 (right only), and Myc-2RD or EV. The cell lysates and Ni^{2+}–pull-down products were immunoblotted with anti-GFP, anti-SPT16, anti–Myc-tag, or anti-actin antibodies as indicated. (**D**) Immunoblot of in vitro ADP-ribosylation of 2RD and histone H3.1 by PARP1. Biotinylated NAD^+ was used as a source of ADP-ribose and immunoblotted with NeutrAvidin protein. (**E**) Immunoblots of in vitro ubiquitination of biotinylated ADP-ribosylated H3.1 tail-GFP ($ADPr_n$-H3.1 tail-GFP) or H3.1 tail-GFP by 2RD. Biotinylated NAD^+ was used as a source of ADP-ribose. Top: Anti-Ub (red) and NeutrAvidin protein. Bottom: Anti-Ub (red) and anti-GFP (green). Asterisk likely denotes a truncated H3.1 tail-GFP fragment (see fig. S2C). (**F**) Immunoblot of in vitro ubiquitination of biotinylated ADP-ribosylated His-HaPARP ($ADPr_n$-His-HaPARP) or His-HaPARP by 2RD performed in the presence of E1, UbcH5B, and Ub. Biotinylated NAD^+ was used as a source of ADP-ribose. Ni^{2+}–pull-down products were immunoblotted with anti-His, anti-Ub, or NeutrAvidin protein as indicated to detect Ub_n-$ADPr_n$-His-HaPARP products.

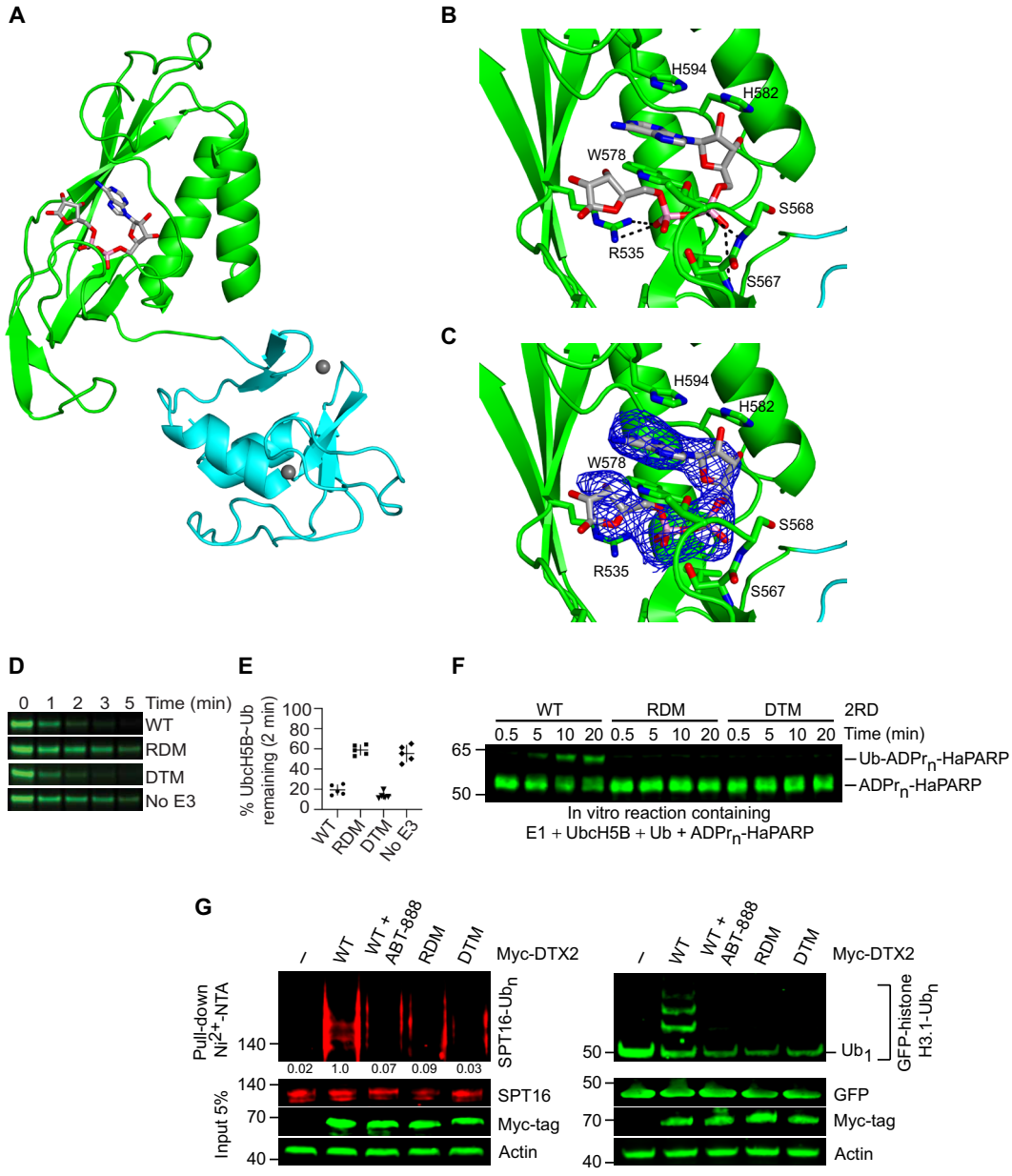

Fig. 4. DTC domain binds ADP-ribosylated substrate. (**A**) Cartoon representation of complex structure of 2RD bound to ADPr, colored and oriented as in Fig. 1B. ADPr is shown in sticks, and C atoms are colored light gray, O atoms are colored red, N atoms are colored blue, and P atoms are colored pink. (**B**) Close-up view of 2RD-ADPr complex. Coloring as in (A) with C atoms from 2RD in the same color as the cartoon representation. Putative hydrogen bonds (2.6 to 3.2 Å) are shown as dashed black lines. (**C**) Close-up view colored and orientated as in (B) with a Polder map (*57*) in blue contoured at 3σ. (**D**) Single-turnover lysine discharge showing the disappearance of UbcH5B~IR-Ub over time with 2RD WT (wild type), RDM (RING double mutant), or DTM (DTC domain triple mutant), or no E3 as indicated. Associated with fig. S3 and table S1. (**E**) Plot showing fraction of UbcH5B~Ub remaining after 2 min of incubation with 2RD variants and lysine as indicated. Data are represented as means ± SD from five replicates. (**F**) Immunoblot of in vitro ubiquitination reactions of biotinylated ADP-ribosylated His-HaPARP by 2RD variants, as indicated and detected with NeutrAvidin protein. Biotinylated NAD^+ was used as a source of ADP-ribose, and all reactions include E1, UbcH5B, and Ub. (**G**) Immunoblots of SPT16 (left) and histone H3.1 (right) ubiquitination by Myc-DTX2 variants in the presence and absence of ABT-888 in HEK293 cells expressing His-Ub, GFP–histone H3.1 (right only), and Myc-DTX2 variant or EV (–); cell lysates and Ni^{2+}–pull-down products were immunoblotted with anti-GFP, anti-SPT16, anti–Myc-tag, or anti-actin antibodies as indicated.

PAR recognition by the DTC domain is conserved

Similarities in the DTC sequences of DTX family proteins suggest that all family members might share the ability to bind PARylated proteins via their DTC domains. This prompted us to investigate whether the DTC domain alone was able to bind PAR. Coimmunoprecipitations of the DTC domains from the different DTX family members and PAR revealed that the DTC domains of all DTX family members bind PAR but not in the presence of ABT-888 (Fig. 5A). These data demonstrate that the DTC domain alone from DTX family Ub ligases is sufficient to bind PARylated proteins.

Because DTX1, DTX2, DTX3L, and DTX4 all have PAR-binding domains at their N and C termini, we reasoned that they might share PARylated substrate interactomes. Using MS-based proteomics on Myc-trap IPs as described earlier, we generated an interaction network for these DTX proteins. Each DTX family E3 has a distinct protein interaction network, and only DTX2 shows a strong association with DDR proteins (Fig. 5B and data S1). We wondered whether these differences could partly be attributed to their cellular localization and thus monitored the localization patterns of these four DTX family E3s using immunocytochemistry. DTX2 was localized mainly in the nucleus, whereas DTX1, DTX3L, and DTX4 were mainly in the cytoplasm (Fig. 5C). These findings suggest that DTX family E3s recognize PARylated substrate through the DTC domain but have distinct interactomes and localization patterns.

DISCUSSION

Members of the DTX family of E3s are characterized by a conserved C terminus composed of a RING and DTC domain. Sequence contiguity of the RING and DTC domains in this family of E3s prompted us to postulate that the DTC domain contributes to substrate recognition and ubiquitination. On the basis of our structures of 2RD and sequence conservation with other DTX proteins, we anticipated that the DTC domain would bind protein substrates via a consensus peptide motif but were surprised to find that the common DTC-binding feature was PAR. Our data reveal that key residues of the ADPr binding site in the DTC domain are strictly conserved in all members of the DTX family and that binding of PARylated targets by the DTC domain requires PARP1/2-mediated PARylation. These results define the DTC domain as a new ADP-ribose–binding module that facilitates PAR-dependent substrate ubiquitination in conjunction with the RING domain.

Although the structure of the DTC domain was initially determined in 2012 (*12*), this is the first instance in which an ADPr binding function has been demonstrated for this domain. In the 2RD-ADPr complex structure, ADPr binds within a DTC pocket that is conserved across the DTX family, and in cells, the DTC domain is sufficient to pull down PARylated targets, regardless from which DTX protein it originates. Furthermore, when we perturb ADPr binding by introducing mutations into this DTC pocket, we abrogate ubiquitination of the model substrate PARylated HaPARP in vitro and reduce ubiquitination of histone H3.1 and SPT16 in cells. The C1″ and C2′ hydroxyl groups of the ribose rings distal and proximal to the adenine ring, respectively, which are required for PAR-chain assembly, are exposed in our 2RD-ADPr complex structure (fig. S4A), suggesting that the DTC domain could bind an ADPr subunit along a linear PAR chain. The C1″ hydroxyl of the ribose distal from the adenine ring also serves as the attachment site of PAR chains to substrate, and its accessibility raises the possibility that the DTC domain could bind to this ADPr subunit in PARylated substrate. Furthermore, the C2′ hydroxyl of the adenine ribose projects into an adjacent pocket (fig. S4A), hinting at the possibility that the DTC domain could prefer another PAR chain pattern. The preferences of the DTX2 DTC domain and whether this varies among DTX family members require further investigation.

Our data illustrate a structural connection in the cross-talk between ADP-ribosylation and ubiquitination, although this is not the first instance of such an example. The RING E3s RNF146 and CHFR respectively harbor a WWE domain and PBZ PAR-binding motif that contributes to the ubiquitination of PARylated substrates (*18*, *26*, *27*). In both E3s, the PAR-binding motifs are distal from the RING domains and function by recruiting PARylated substrates for ubiquitination by the RING domain. For RNF146, ubiquitination also depends on *iso*-ADPr binding to the WWE domain to induce a conformational change in the RING domain to facilitate E2~Ub binding (*25*). In DTX2, the DTC domain is linked to the RING domain, where ubiquitination is contingent on recruitment of ADP-ribosylated substrate by the DTC domain, presumably to bring substrate proximal to the E2~Ub binding site on the RING domain. The structural configuration of the RING-DTC motif suggests that efficient ubiquitination likely occurs when the DTC domain engages with an ADPr subunit close to the substrate-PAR linkage site such that the RING domain–bound E2~Ub could reach substrate lysine sites. Thus, it seems likely that it might favor mono- or short poly-ADP-ribose modified substrates.

Four of the five DTX family members have a second method of binding PAR chains via tandem WWE domains or a binding partner. We confirmed that the tandem WWE domains from DTX2 are competent in binding PARylated substrates. However, our mutagenesis analyses of the DTC and tandem WWE domains show that the DTC domain plays the prominent role in recruiting PARylated substrates for ubiquitination. Our 2RD structures show that the RING domain is connected to the DTC domain by a five-residue linker. While this linker allows some degree of rotational flexibility between these two domains, the proximity of the RING and DTC domains could influence or limit substrate accessibility to RING domain–bound E2~Ub such that ubiquitination preferentially occurs on PARylated substrates bound via the DTC domain. Given that the tandem WWE domains also bind PARylated substrates, what might be their role? A model of the tandem WWE domains from *D. melanogaster* Dtx protein bound to two molecules of *iso*-ADPr based on the structure of RNF146 WWE domain bound to *iso*-ADPr suggests that the two *iso*-ADPr binding sites in the Deltex tandem WWE domain are joined together (fig. S4B), thereby creating a larger pocket that could exhibit a preference for a yet unidentified pattern of PAR. It is tempting to speculate that the tandem WWE domains might display high affinity for a particular PAR pattern that serves as the initial step of PARylated substrate recruitment to cooperate with RING-DTC domain in ubiquitination. Further studies are required to determine how the tandem WWE and DTC domains coordinate to bind PARylated substrate for ubiquitination.

Given that PARylation and ubiquitination are critical for communicating signals between proteins to produce desired outcomes, this newly identified PAR-binding role of the DTC domain from the DTX family of E3 Ub ligases establishes another mechanism for cross-talk between these two modifications. Despite the similarities in the RING and DTC domains of DTX E3s, our data reveal that DTX2 predominantly associates with PARP1 and other PARylated DDR proteins. PARylation and Ub-mediated degradation of DNA damage proteins frequently occur as concerted events during DDR (*18*, *20*) and whether DTX2 has a role in the DDR pathway merits further investigation. Because DTX family members have distinct interactomes, characterizing the role of PAR binding by the DTC domain will provide insights into their functions. Future studies are required to fully characterize the PARylation requirements for substrate ubiquitination and the role of this PARylation-ubiquitination cross-talk in DTX-modulated pathways.

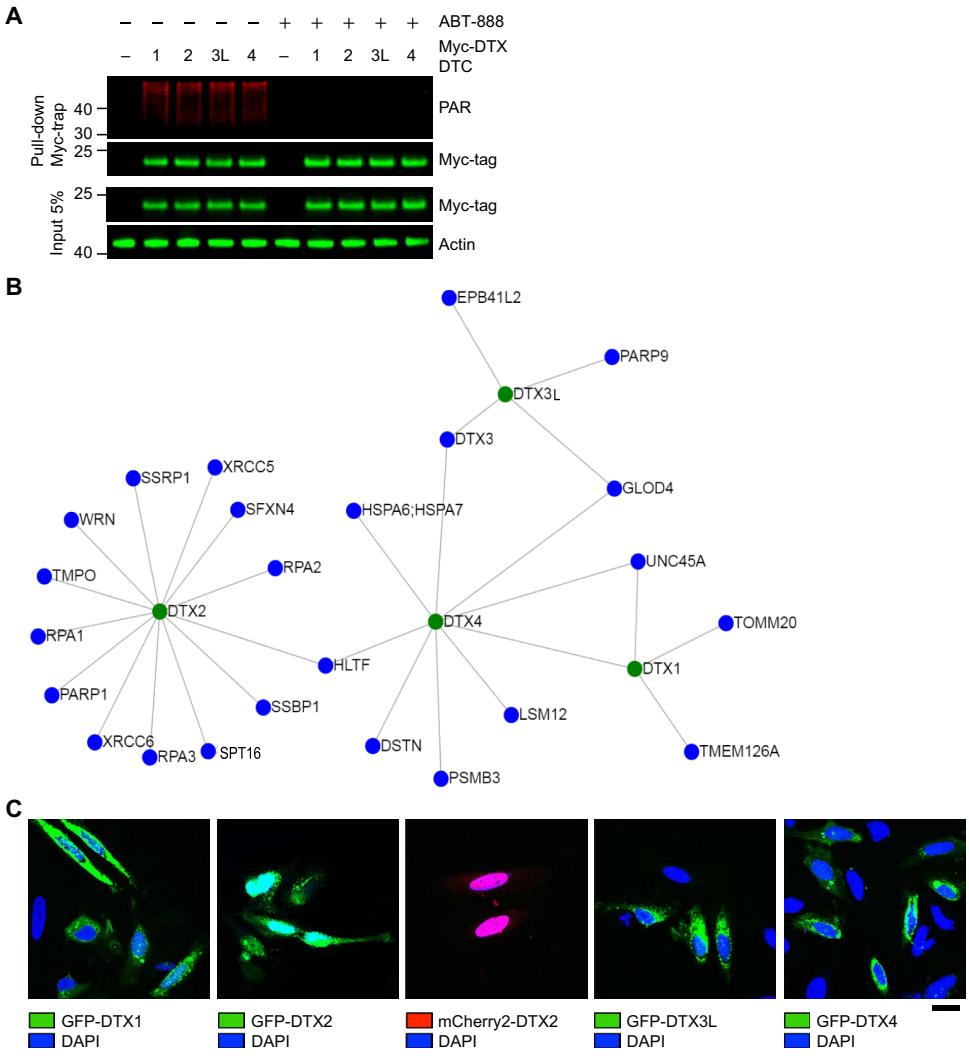

Fig. 5. Characterization of DTX family E3s. (**A**) Immunoblots of Myc-trap pull-downs of whole-cell lysates from HEK293 cells expressing EV (–) or Myc-tagged DTC domains from DTX1, DTX2, DTX3L, or DTX4 in the presence and absence of ABT-888 using anti-PAR, anti–Myc-tag, or anti-actin as indicated. (**B**) Network of DTX protein interactors generated from MS analyses of Myc-trap pull-downs of individual DTX family members. Label-free quantification (LFQ) intensities using the Hawaii plot functionality in Perseus were used to generate the networks. Associated with data S1. (**C**) Merged images from HeLa cells overexpressing GFP-DTX1, GFP-DTX2, mCherry-DTX2, GFP-DTX3L, or GFP-DTX4 as indicated. Cells on coverslips were fixed and mounted on glass slides using the nuclear stain DAPI (4′,6-diamidino-2-phenylindole). The scale bar (bottom right) represents 20 μm in each panel.

MATERIALS AND METHODS

Mammalian cell lines

The mammalian cells used in this study are HEK293 and HeLa (cervical cancer). The HEK293 cells were grown in Dulbecco's modified Eagle medium (DMEM), while the HeLa cells were grown in RPMI. The media were supplemented with 10% fetal bovine serum, streptomycin (0.1 mg/ml), penicillin (100 U/ml), and Gibco gentamicin reagent (6 μg/ml; ThermoFisher Scientific). DMEM and RPMI media were further supplemented with 20 mM L-glutamine. Cells were cultured in monolayer in 5% CO_2 at 37°C. The cell lines were purchased from the American Type Culture Collection (ATCC) or German Collection of Microorganisms and Cell Cultures (DSMZ), revived, and sent for in-house cell line authentication by short tandem repeat profiling using GenePrint 10 System (Promega). The cell lines already in stock are authenticated every 2 years, and the cells in culture are also tested for mycoplasma through a rota-basis (~every 6 months) in-house or earlier if required.

Construct generation

New constructs were generated using standard polymerase chain reaction–ligation techniques and verified by automated sequencing. GST-tagged constructs were cloned into pGEX4T-1 (GE Healthcare) modified with a Tobacco etch virus (TEV) cleavage site and an N-terminal uncleavable His-tag (pGEX4T1 HG TEV) or pGEX4T-3 modified with a TEV cleavage site and a second ribosomal binding and multiple cloning site (pABLO TEV). Constructs with an N-terminal His-tag were cloned into pRSFDuet-1 (Novagen) modified with a TEV cleavage site following the N-terminal His-tag (pRSFDuet TEV) or into pRSFDuet TEV in which the N-terminal 6× His-tag has been replaced with a 12× His-tag (pRSFDuet 12× His TEV). DNA

encoding the histone H3.1 tail (residues 1 to 43) was cloned into modified pRSFDuet-1 (Novagen), in which the N-terminal His-tag was deleted and the Xho I site was followed by a TEV cleavage site and GFP–His-tag. DNA encoding PARP1 and its variant was cloned into pET-21a(+) (Novagen) in-frame with the uncleavable C-terminal His-tag. For His-Ub, DNA encoding MHHHHHH-Ub was cloned into pET-3a (Novagen); for IR-Ub, DNA encoding GGSC-Ub was cloned into pGEX4T1 HG TEV. Mammalian constructs were cloned into pcDNA3 modified with an N-terminal Myc-tag (pcDNA3Myc), pGZdx21Z (*28*), pcDNA3.1 B(+), or mCherry2-C1, a gift from M. Davidson (Addgene plasmid no. 54563).

Protein expression and purification

Escherichia coli BL21(λDE3) GOLD cells were used for the expression of recombinant proteins. Cells were grown at 37°C in Luria-Bertani medium until reaching an OD_{600} (optical density at 600 nm) of 0.6 to 0.8. Expression was then induced with 0.2 mM isopropyl β-D-1-thiogalactopyranoside at 18° to 20°C for 12 to 16 hours. Following expression, bacterial cells were harvested by centrifugation and lysed with a microfluidizer or sonicator. Cells expressing GST-tagged proteins were resuspended in 200 mM NaCl, 50 mM tris-HCl (pH 7.6), 1 mM dithiothreitol (DTT), and 2.5 mM phenylmethylsulfonyl fluoride (PMSF), and cells expressing His-tagged proteins (including H3.1 tail-GFP) were resuspended in 200 mM NaCl, 25 mM tris-HCl (pH 7.6), 15 mM imidazole, 5 mM β-mercaptoethanol (BME), and 2.5 mM PMSF, or, in the case of His-HaPARP variants, in 300 mM NaCl, 25 mM tris-HCl (pH 8), 15 mM imidazole, 5 mM BME, and 2.5 mM PMSF. Cell lysates were cleared by high-speed centrifugation.

To purify DTX2, its variants, H3.1 tail-GFP and His-Ub, clarified lysates were applied to glutathione affinity or Ni^{2+}-agarose, depending on the tag system, using a gravity column or by incubating for 1 to 2 hours on a rotary shaker at 4°C. Resins were washed in buffers similar to the lysis buffer; GST-tagged proteins were eluted in 50 mM tris-HCl (pH 8.0), 200 mM NaCl, 1 mM DTT, 10 mM glutathione, and His-tagged proteins in 25 mM tris-HCl (pH 7.6), 200 mM NaCl, 5 mM BME, and 200 mM imidazole. H3.1 tail-GFP was buffer-exchanged into 300 mM NaCl, 25 mM Hepes (pH 8), and 0.1 mM (tris(2-carboxyethyl)phosphine) (TCEP). All the other tagged proteins were further purified by size exclusion chromatography on a Superdex 75 or Superdex 200 column (GE Healthcare) equilibrated in 150 mM NaCl, 25 mM tris-HCl (pH 7.6), and 1 mM DTT before snap-freezing in liquid nitrogen and storing at −80°C.

For removal of tags, protein samples were dialyzed against 25 mM tris-HCl (pH 7.6), 150 mM NaCl, and 5 mM BME overnight at 4°C in the presence of TEV protease. The proteins of interest were separated from the affinity tags or the remaining uncleaved proteins by applying the dialyzed and cleaved samples onto the same resin and collecting the flow-through. Further purification was performed by size exclusion chromatography on a Superdex 75 column (GE Healthcare), pre-equilibrated in 25 mM tris-HCl (pH 7.6), 150 mM NaCl, and 1 mM DTT.

To purify His-HaPARP, clarified lysate was applied to a High Density Nickel Resin (Agarose Bead Technologies) gravity column; washed with 1 M NaCl, 25 mM tris-HCl (pH 8), 15 mM imidazole, and 5 mM BME, followed by 300 mM NaCl, 25 mM tris-HCl (pH 8), 15 mM imidazole, and 5 mM BME; and eluted with 300 mM NaCl, 25 mM tris-HCl (pH 8), 300 mM imidazole, and 5 mM BME. His-HaPARP was dialyzed against 300 mM NaCl, 25 mM tris-HCl (pH 8), and 1 mM DTT before snap-freezing in liquid nitrogen and storing at −80°C.

To purify IR-Ub for labeling, clarified lysate from cells expressing HisGST-TEV-GGSC-Ub was applied onto a glutathione agarose resin column and washed in lysis buffer described above but with 5 mM DTT. TEV protease and lysis buffer were added to the column, and GGSC-Ub was cleaved at 4°C overnight using a circular system and a peristaltic pump. The flow-through was collected and applied onto a Superdex 75 26/60 column (GE Healthcare) equilibrated in phosphate-buffered saline (PBS).

Other proteins were purified using previously described protocols: *Arabidopsis thaliana* Uba1 (AtUba1) and UbcH5B S22R (*29*, *30*), UbcH5B (*30*, *31*), untagged Ub for Fig. 4E (*30*, *32*), and stably conjugated UbcH5B C85K S22R–Ub (*30*, *33*). PARP1-His was purified as described (*34*) but without gel filtration chromatography. Protein concentrations were determined either by measurement of the absorbance at 280 nm based on molar extinction coefficients calculated from the relevant sequences using ExPASy's ProtParam (*35*) or by Bradford assay using bovine serum albumin (BSA) as a standard.

SPR binding assays

The SPR experiments were performed with CM-5 chips (GE Healthcare) on a Biacore T200 at 25°C. GST and GST-tagged proteins were captured onto a CM-5 chip coupled with anti-GST to 1000 to 2000 response units. UbcH5B S22R C85K–Ub and UbcH5B S22R were serially diluted in running buffer [25 mM tris-HCl (pH 7.6), 150 mM NaCl, BSA (0.1 mg/ml), 1 mM DTT, and 0.005% (v/v) Tween 20] to concentration ranges of 0 to 100 μM to measure binding. Differences in signal between GST-protein and GST alone are reported, and representative sensorgrams were prepared in GraphPad Prism (version 8.1.0).

Crystallization

Purified His-2RD or 2RD was concentrated to ~10 mg/ml and screened in sitting drop vapor diffusion trays. Crystals of form 1 (His-2RD) and form 2 (2RD) were obtained in 0.1 M tris-HCl (pH 7.6), 36% glycerol ethoxylate, and Morpheus condition 60 (Molecular Dimensions), respectively. For the complex bound to ADPr, 2RD crystals similar to form 1 were obtained in Morpheus condition 39 (Molecular Dimensions) and soaked in 10 mM ADPr for 30 s.

Data collection and structure determination

Data were collected at Diamond Light Source (DLS) beamlines I03 and I04 and processed using the xia2 pipeline (*36*), including DIALS (*37*), POINTLESS (*38*), and AIMLESS (*39*). The structure of 2RD form 1 was determined using the fast_ep pipeline at DLS. The poly-Ala model was extended and corrected using COOT. The structures of 2RD form 2 and 2RD-ADPr complex were determined by molecular replacement using the structure of 2RD form 1 as the search model with PHASER (*40*). The structures were refined in BUSTER (*41*) or PHENIX (*42*) and manually inspected in COOT. TLS parameterization was used throughout. The final models were validated using MolProbity (*43*). All data processing and refinement statistics are presented in Table 1. Superimpositions and protein surface areas were respectively calculated in LSQMAN (*44*) and PISA (*45*), and figures were made in PyMOL (www.pymol.org). The Polder density map in Fig. 4C was calculated in PHENIX. Electrostatic surface potentials were calculated using PDB2PQR and APBS (*46*).

Interactome and Ub remnant sample preparations

For preparing samples for the determination of interactomes of different DELTEX proteins, EV and Myc-tagged full-length DTX1,

DTX2, DTX3L, and DTX4 were expressed in HEK293 cells and pulled down with Myc-trap (Chromotek) in triplicate experiments. The beads were washed twice with IP lysis buffer and once each with IP wash buffer and high-performance liquid chromatography–grade water, and processed following a previously established protocol (*47*). Digestion of samples was performed by subsequent use of both endoLysC and trypsin in AMBIC. For preparing samples for Ub remnant motif analysis of DTX2-ubiquitinated substrate peptides using PTMScan Ubiquitin Remnant Motif (K-ε-GG) Kit (Cell Signaling Technology, catalog no. 5562), EV and GFP-DTX2 were overexpressed in HEK293 cells in triplicate plates, induced with 50 μM H_2O_2 (Sigma-Aldrich) for 10 min, and further treated with MG132 (Sigma-Aldrich) for 4 hours. Lysates were prepared and processed following the manufacturer's protocol.

MS data collection and processing

Peptides resulting from all trypsin digestions were separated by nanoscale C18 reverse-phase liquid chromatography using EASY-nLC II 1200 (ThermoFisher Scientific) coupled to an Orbitrap Fusion Lumos mass spectrometer (ThermoFisher Scientific). Elution was carried out at a flow rate of 300 nl/min using a binary gradient, into a 50-cm fused silica emitter (New Objective) packed in-house with ReproSil-Pur C18-AQ, 1.9-μm resin (Dr. Maisch GmbH), for a total run time duration of 135 min. The packed emitter was kept at 50°C by means of a column oven (Sonation) integrated into the Thermo Scientific Nanospray Flex ion source from which eluting peptides were electrosprayed into the mass spectrometer. An Active Background Ion Reduction Device (ESI Source Solutions) was used to decrease air contaminant signals. Xcalibur software (ThermoFisher Scientific) was used for data acquisition. A full scan over a mass range of 350 to 1400 mass/charge ratio (*m*/*z*) was acquired at 120,000 resolution at 200 *m*/*z*. Higher-energy collisional dissociation fragmentation was performed on the 15 most intense ions, and peptide fragments generated were analyzed in the Orbitrap at 15,000 resolution.

The MS raw data were processed with MaxQuant software version 1.6.3.3 (*48*), and peptides were identified with the Andromeda search engine (*49*), querying Swiss-Prot (*50*) *Homo sapiens* (30/04/2019; 42411 entries). First and main searches were performed with precursor mass tolerances of 20 and 4.5 parts per million (ppm), respectively, and an MS/MS tolerance of 20 ppm. The minimum peptide length was set to six amino acids, and specificity for trypsin cleavage was required. Methionine oxidation and N-terminal acetylation were specified as variable modifications, whereas cysteine carbamidomethylation was set as a fixed modification. For the Ub remnant experiment, GlyGly-Lys was included as a variable modification. The peptide, protein, and site false discovery rate (FDR) was set to 1%. All MaxQuant outputs were analyzed with Perseus software version 1.6.2.3 (*51*).

Transfections, coimmunoprecipitation, and Western blotting

Lipofectamine 2000 (ThermoFisher Scientific) or Polyplus (Polyplus-transfection) reagents were used to transfect the cell lines with the plasmids following the manufacturers' protocols. Unless otherwise mentioned, cells were harvested 48 hours after transfection. Cells were resuspended in IP lysis buffer [50 mM tris-HCl (pH 7.5), 150 mM NaCl, 1 mM EDTA, 1% IGEPAL CA-630, 10% glycerol, 0.5 mM DTT, and protease inhibitor cocktail] to prepare whole-cell lysates for Western blot and IP as described previously (*52*). For IP using Myc-trap (Chromotek), the lysates were incubated for 1 hour with the respective traps. The beads were washed twice with IP lysis buffer and once with IP wash buffer (IP lysis buffer consisting of 200 mM NaCl and 1.0 mM DTT). In addition, all lysis and incubation buffers for IPs and pull-downs contained 2 μM ABT-888 (Santa Cruz Biotechnology) to inhibit PARylation of substrates during lysis. Immunoprecipitated proteins were eluted in 40 μl of 2× loading dye at 95°C. Immunoblotting was performed as described previously (*52*) with some modifications. Protein samples were separated by SDS–polyacrylamide gel electrophoresis (SDS-PAGE) in NuPAGE 4 to 12% bis-tris precast gels using either MES SDS or Mops SDS running buffer. The samples were then transferred onto nitrocellulose membranes from Trans-Blot Turbo Transfer Packs using a Trans-Blot Turbo transfer system. The immunoblots were scanned on the Odyssey CLx Imaging System (LI-COR Biosciences). Actin was used as a loading control in the immunoblots from cell-based assays. For Fig. 2B, multiple gels were run under similar conditions to probe all the target proteins through immunoblotting and actin presented is representative of all the actins probed for each separate gel. The following dilutions of primary antibodies have been used in immunoblotting: rabbit anti-PARP1 (1:1000; Cell Signaling Technology, catalog no. 9532), rabbit anti-SPT16 (1:1000; Cell Signaling Technology, catalog no. 12191), rabbit anti-SSRP1 (1:1000; Cell Signaling Technology, catalog no. 13421), rabbit anti-XRCC5 (1:1000; Cell Signaling Technology, catalog no. 2180), rabbit anti-XRCC6 (1:1000; Cell Signaling Technology, catalog no. 4104), rabbit anti-RPA1 (1:1000; Cell Signaling Technology, catalog no. 2267), mouse anti-Myc tag (1:1000; Cell Signaling Technology, catalog no. 2276), goat anti-actin (1:1000; Santa Cruz Biotechnology, catalog no. sc-1616), mouse anti-GFP (1:1000; Santa Cruz Biotechnology, catalog no. sc-81045), mouse anti–histone H3.1 (1:1000; Cell Signaling Technology, catalog no. 14269), mouse anti–His-tag (1:1000; ThermoFisher Scientific, catalog no. MA1-21315), rabbit anti-PAR (1:500; Merck, catalog no. MABC547), mouse anti-GFP (1:1000; Cell Signaling Technology, catalog no. 2955), rabbit anti-Ub (1:1000; Sigma-Aldrich, catalog no. 662099), or mouse anti-Ub (1:1000; Cell Signaling Technology, catalog no. 3936). The secondary antibodies used are as follows: goat anti-mouse IRDye 800CW (1:15,000; LI-COR Biosciences, catalog no. 925-32210), goat anti-rabbit IRDye 680LT (1:20,000; LI-COR Biosciences, catalog no. 925-68021), goat anti-mouse IRDye 680LT (1:20,000; LI-COR Biosciences, catalog no. 925-68020), goat anti-rabbit IRDye 800CW (1:15,000; LI-COR Biosciences, catalog no. 026-32211), donkey anti-goat IRDye 800CW (1:15,000; LI-COR Biosciences, catalog no. 925-32214), or NeutrAvidin Protein, DyLight 800 (1:15,000; ThermoFisher Scientific, catalog no. 22832).

Labeling IR-Ub

GGSC-Ub was incubated with a 1.2-fold molar excess of IRDye 800CW Maleimide (LI-COR Biosciences) for 2.5 hours at room temperature in the dark and subsequently buffer-exchanged into 150 mM NaCl and 25 mM tris-HCl (pH 7.6) by passing the mixture consecutively over two Zeba Spin Desalting columns (ThermoFisher Scientific). The concentration of labeled Ub was estimated on the basis of a 95% recovery rate per desalting column. A 20:1 molar ratio of unlabeled-to-labeled GGSC-Ub was used for assays.

In vitro ADP-ribosylation and ubiquitination assays

For Fig. 2E, *A. thaliana* Ub-activating enzyme E1 (AtUba1; 1 μM) was used to charge UbcH5B (10 μM) with IR-Ub (100 μM) for 2 min

at room temperature in 50 mM NaCl, 50 mM tris-HCl (pH 7.6), 5 mM $MgCl_2$, and 5 mM ATP. GST-2RD (2.5 μM) and ABT-888 [10 μM; 600 μM stock in dimethyl sulfoxide (DMSO)] or DMSO (3.3%, v/v) were added, and aliquots were removed at indicated time points and quenched with 4× NuPAGE LDS Sample Buffer (Invitrogen). Samples were reduced with 125 mM DTT for 5 min at room temperature before separating components with SDS-PAGE. Gels were visualized by staining with InstantBlue (Expedeon) after scanning with the Odyssey CLx Imaging System (LI-COR Biosciences).

For Fig. 3D, PARP1-His (1 μM), duplex activating DNA (0.5 μM), NAD^+ (50 μM), biotinylated NAD^+ (12.5 μM; Trevigen), ABT-888 (10 μM), histone H3.1 (0.75 μM; New England Biolabs, M2503), and 2RD (0.75 μM) were incubated at 23°C for 1 hour. Reactions were quenched with gel-loading dye. Samples were immunoblotted against NeutrAvidin Protein, DyLight 800 to identify biotinylated ADP-ribosylated products.

For Fig. 3E, H3.1 tail-GFP (20 μM), PARP1 E988Q (1 μM), duplex activating DNA (0.5 μM), NAD^+ (100 μM), and biotinylated NAD^+ (12.5 μM; BIOLOG Life Science Institute) were incubated for 1 hour at 30°C in 25 mM NaCl, 50 mM Hepes (pH 7.5), 5 mM $MgCl_2$, and 1 mM TCEP and subsequently buffer-exchanged into 150 mM NaCl and 25 mM Hepes (pH 7.5) with Zeba Spin Desalting columns (ThermoFisher Scientific) to generate biotinylated ADP-ribosylated H3.1 tail-GFP. For unmodified H3.1 tail-GFP, NAD^+ and biotinylated NAD^+ were omitted. Ubiquitination reactions were performed for 0.5 hour at 21°C with AtUba1 (0.4 μM), UbcH5B (10 μM), Ub (100 μM), 2RD (1 μM), and H3.1 tail-GFP or biotinylated ADP-ribosylated H3.1 tail-GFP (9.6 μM) in 50 mM NaCl, 50 mM tris-HCl (pH 7.6), 5 mM $MgCl_2$, and 5 mM ATP. Reactions were quenched with NuPAGE LDS Sample Buffer (Invitrogen) containing 250 mM DTT. Samples were immunoblotted against mouse anti-GFP and rabbit anti-Ub or mouse anti-Ub and NeutrAvidin Protein, DyLight 800.

For Figs. 3F and 4F, His-HaPARP (5 μM), calf thymus DNA (0.05 mg/ml; Sigma-Aldrich), NAD^+ (50 μM), and biotinylated NAD^+ (12.5 μM; Trevigen) were incubated for 1 hour at 23°C in 25 mM NaCl, 50 mM Hepes (pH 7.5), 5 mM $MgCl_2$, and 1 mM TCEP and subsequently buffer-exchanged into 150 mM NaCl, 25 mM tris-HCl (pH 7.6) or 150 mM NaCl, 25 mM Hepes (pH 7.5) with Zeba Spin Desalting columns (ThermoFisher Scientific) to generate biotinylated ADP-ribosylated His-HaPARP for ubiquitination assays. For His-HaPARP without ADP-ribosylation, either calf thymus DNA or calf thymus DNA and NAD^+/biotinylated NAD^+ were omitted.

For Fig. 3F, ubiquitination reactions were performed for 1 hour at 25°C in conditions identical to those described for Fig. 3E but with His-HaPARP or biotinylated ADP-ribosylated His-HaPARP (2.6 μM). Reactions were subsequently incubated with Dynabeads His-tag matrix (Invitrogen) at 4°C for 30 min; washed with 0.3 M NaCl, 50 mM phosphate (pH 8), and 0.01% Tween-20; and eluted in wash buffer containing 300 mM imidazole. Samples were prepared with gel-loading dye containing 250 mM DTT and immunoblotted against NeutrAvidin Protein, DyLight 800 or mouse anti-His and rabbit anti-Ub.

For Fig. 4F, ubiquitination reactions were performed and quenched as described for Fig. 3E but with biotinylated ADP-ribosylated His-HaPARP (2.1 μM), BSA (0.2 mg/ml), and GST-2RD variants (0.9 μM). Samples were immunoblotted against NeutrAvidin Protein, DyLight 800.

For the in vitro ADP-ribosylation and ubiquitination assays, samples were separated by SDS-PAGE in Mops running buffer, and gels and immunoblots were visualized by scanning with the Odyssey CLx Imaging System (LI-COR Biosciences). Final concentrations are in parentheses.

In vitro single-turnover lysine discharge assays

AtUba1 (0.4 μM) was used to charge UbcH5B (20 μM) with IR-Ub (30 μM) for 15 min at 23°C in 50 mM tris-HCl (pH 7.6), 50 mM NaCl, 5 mM $MgCl_2$, and 5 mM ATP. Charging was stopped by incubating the reaction with 50 mM EDTA for 1 to 2 min. Discharge was initiated by the addition of a mixture containing L-lysine (130 mM) and GST-2RD variant (1.1 μM). Reactions were quenched at indicated times with 4× loading dye and resolved by SDS-PAGE. Gels were visualized using the Odyssey CLx Imaging System (LI-COR Biosciences). Final concentrations are in parentheses except for UbcH5B and IR-Ub, which were 7.5 and 11.25 μM, respectively.

In vitro pull-down of PARylated PARP1-His

PARP1-His (2.1 μM) was incubated with duplex activating DNA (0.5 μM) and NAD^+ (100 μM) for 1 hour at 30°C. For unPARylated samples, NAD^+ was omitted. Reactions were buffer-exchanged into wash buffer [0.2 M NaCl, 50 mM tris-HCl (pH 7.6), 1 mM DTT, 1 mM EDTA, and 0.5% IGEPAL CA-630] with Zeba Spin Desalting columns (ThermoFisher Scientific). Equimolar amounts of GST or GST-DTX2 WWE were incubated with Glutathione Agarose-4B Resin (Agarose Bead Technologies) and 15 μg of PAR-PARP1-His or PARP1-His, washed in wash buffer, and eluted with 1× gel-loading dye containing 50 mM DTT. Samples were separated by SDS-PAGE in Mops running buffer and visualized by staining with InstantBlue (Expedeon) or immunoblotting against anti-PAR (1:1000) and anti-PARP1 and scanning with the Odyssey CLx Imaging System (LI-COR Biosciences).

Cell-based ubiquitination assays

The ubiquitination assays from mammalian whole-cell lysates were performed under denaturing condition. HEK293 cells were transfected with His-Ub and other plasmids to overexpress the proteins as indicated in the figures. Twenty-four hours after transfection, the cells were treated with 50 μM ABT-888 as indicated in the figures. The cells were harvested after 36 hours following treatment with 50 μM MG132 for 4 hours. In Figs. 3B and 4G, the cells were treated with 50 μM H_2O_2 for 30 min before MG132 treatment. Five percent of the cells were kept as separate pellets; the remaining were suspended in 750 μl of lysis buffer UBA [8 M urea, 0.3 M NaCl, 50 mM phosphate (pH 8.0), and *N*-ethylmaleimide (NEM; 100 μg/ml)] and sonicated. Lysate concentrations were estimated using a NanoDrop spectrophotometer (Denovix), and each lysate was normalized to a volume of 1 ml to have equal concentrations. Dynabeads His-tag matrix (Invitrogen) was added to the lysates and incubated on a rotatory shaker at 4°C overnight. The beads were washed with UBA, UBB, UBC, and PBS [UBB = UBA and UBC 1:1; UBC = 0.3 M NaCl, 50 mM phosphate (pH 8.0), NEM (100 μg/ml)] and eluted in 2× protein loading dye by incubating at 95°C for 10 min. Lysates from the saved pellet was prepared in IP lysis buffer. The eluted samples and whole-cell lysates were resolved using SDS-PAGE and immunoblotted with the antibodies as indicated in the figures.

Immunocytochemistry

The cells (overexpressing GFP or mCherry-tagged proteins) on coverslips were washed thrice with PBS and fixed in methanol. The coverslips were then mounted onto glass slides containing VECTASHIELD

antifade mounting medium (Vector Laboratories) and sealed. The images were captured on a Zeiss 710 upright confocal microscope at ×60 (oil) magnification.

Quantification and statistical analysis

For the affinity purification MS experiment, protein abundance was measured using the label-free quantification (LFQ) algorithm available in MaxQuant (*53*) and is reported in data S1. Only proteins quantified in all three replicates in at least one group were kept for downstream analysis. Missing values were imputed separately for each column (width, 0.3; down shift, 1.8), and significantly enriched proteins were selected using a *t* test with a 5% FDR (permutation-based) and reported in data S1. Only significantly enriched proteins in which $\log_2$ (Myc-DTX2/EV) > 0 were considered for further evaluation/validation and colored in the volcano plot.

Networks of DTX protein interactors were generated from LFQ intensities using the Hawaii plot functionality in Perseus (*54*). Different s0 and FDR% parameters were used in the multi-volcano analysis to define class A (higher confidence, s0 = 1, FDR = 0.01%) and class B (lower confidence, s0 = 1, FDR = 0.2%) potential interactors. The generated data (data S1) were imported into Cytoscape 3.7.2 (*55*) for network visualization.

The MaxQuant output GlyGly-Lys file (data S2) was used for quantification of ubiquitinated peptides. Reverse and potential contaminant flagged peptides were removed. Missing values were imputed separately for each column (width, 0.3; down shift, 1.8). Only ubiquitinated peptides that had a "score diff" greater than 5, had a localization probability higher than 0.75, and were robustly quantified in all three replicate experiments were included in the analysis. To determine significantly changing ubiquitinated peptides, a Student's *t* test with a 1% FDR (permutation-based) was applied to the peptide intensities included in data S2. For the volcano analysis, s0 and FDR% were 0.5 and 1%, respectively. Ubiquitinated peptides from proteins annotated in the Gene Ontology database with the term "DNA repair" are highlighted in Fig. 2C. Only ubiquitinated peptides more abundant in the lysates from cells expressing GFP-DTX2 were considered for further evaluation/validation and only the DNA repair peptides from this set are colored in the volcano plot.

For SPR assays, Biacore T200 BIAevaluation software (GE Healthcare) was used for the analyses of data by steady-state affinity for 2RD variants. The number of replicates (n) for each K_d (presented as mean) ± SEM measurement is indicated in fig. S3 and table S1.

For single-turnover lysine discharge assays (Fig. 4, D and E), data are presented as an average ± SD based on five replicates for each measurement. Image Studio software (version 5.2.5; LI-COR Biosciences) was used to quantify the intensity of each band (I), and GraphPad Prism (version 8.1.0) was used to generate the plot. The % UbcH5B~Ub remaining was calculated using the following equation

$$\%\text{UbcH5B}\sim\text{Ub remaining} = 100 * I_{t=2\ \text{min}} / I_{t=0\ \text{min}}$$

In Fig. 4G, the ubiquitinated SPT16 species under different conditions from two replicates were quantified using the LI-COR Image Studio Lite software, and values assigned for each band are relative to DTX2 WT. For immunocytochemistry and immunoblotting data, representative images and blots were shown in the figures and the experiments were performed in triplicate unless otherwise mentioned.

SUPPLEMENTARY MATERIALS

Supplementary material for this article is available at http://advances.sciencemag.org/cgi/content/full/6/34/eabc0629/DC1

View/request a protocol for this paper from *Bio-protocol*.

REFERENCES AND NOTES

1. A. Hershko, A. Ciechanover, The ubiquitin system. *Annu. Rev. Biochem.* **67**, 425–479 (1998).
2. D. Komander, M. Rape, The ubiquitin code. *Annu. Rev. Biochem.* **81**, 203–229 (2012).
3. R. J. Deshaies, C. A. Joazeiro, RING domain E3 ubiquitin ligases. *Annu. Rev. Biochem.* **78**, 399–434 (2009).
4. B. T. Dye, B. A. Schulman, Structural mechanisms underlying posttranslational modification by ubiquitin-like proteins. *Annu. Rev. Biophys. Biomol. Struct.* **36**, 131–150 (2007).
5. N. Kishi, Z. Tang, Y. Maeda, A. Hirai, R. Mo, M. Ito, S. Suzuki, K. Nakao, T. Kinoshita, T. Kadesch, C.-c. Hui, S. Artavanis-Tsakonas, H. Okano, K. Matsuno, Murine homologs of deltex define a novel gene family involved in vertebrate Notch signaling and neurogenesis. *Int. J. Dev. Neurosci.* **19**, 21–35 (2001).
6. K. Takeyama, R. C. T. Aguiar, L. Gu, C. He, G. J. Freeman, J. L. Kutok, J. C. Aster, M. A. Shipp, The BAL-binding protein BBAP and related Deltex family members exhibit ubiquitin-protein isopeptide ligase activity. *J. Biol. Chem.* **278**, 21930–21937 (2003).
7. P. Chastagner, E. Rubinstein, C. Brou, Ligand-activated Notch undergoes DTX4-mediated ubiquitylation and bilateral endocytosis before ADAM10 processing. *Sci. Signal.* **10**, eaag2989 (2017).
8. D. Choi, E. Park, E. Jung, Y. J. Seong, J. Yoo, E. Lee, M. Hong, S. Lee, H. Ishida, J. Burford, J. Peti-Peterdi, R. H. Adams, S. Srikanth, Y. Gwack, C. S. Chen, H. J. Vogel, C. J. Koh, A. K. Wong, Y.-K. Hong, Laminar flow downregulates Notch activity to promote lymphatic sprouting. *J. Clin. Invest.* **127**, 1225–1240 (2017).
9. K. Matsuno, R. J. Diederich, M. J. Go, C. M. Blaumueller, S. Artavanis-Tsakonas, Deltex acts as a positive regulator of Notch signaling through interactions with the Notch ankyrin repeats. *Development* **121**, 2633–2644 (1995).
10. Q. Yan, S. Dutt, R. Xu, K. Graves, P. Juszczynski, J. P. Manis, M. A. Shipp, BBAP monoubiquitylates histone H4 at lysine 91 and selectively modulates the DNA damage response. *Mol. Cell* **36**, 110–120 (2009).
11. Q. Yan, R. Xu, L. Zhu, X. Cheng, Z. Wang, J. Manis, M. A. Shipp, BAL1 and its partner E3 ligase, BBAP, link poly(ADP-ribose) activation, ubiquitylation, and double-strand DNA repair independent of ATM, MDC1, and RNF8. *Mol. Cell. Biol.* **33**, 845–857 (2013).
12. J. Obiero, J. R. Walker, S. Dhe-Paganon, Fold of the conserved DTC domain in Deltex proteins. *Proteins* **80**, 1495–1499 (2012).
13. M. E. Zweifel, D. J. Leahy, D. Barrick, Structure and Notch receptor binding of the tandem WWE domain of Deltex. *Structure* **13**, 1599–1611 (2005).
14. L. Aravind, The WWE domain: A common interaction module in protein ubiquitination and ADP ribosylation. *Trends Biochem. Sci.* **26**, 273–275 (2001).
15. F. He, K. Tsuda, M. Takahashi, K. Kuwasako, T. Terada, M. Shirouzu, S. Watanabe, T. Kigawa, N. Kobayashi, P. Güntert, S. Yokoyama, Y. Muto, Structural insight into the interaction of ADP-ribose with the PARP WWE domains. *FEBS Lett.* **586**, 3858–3864 (2012).
16. Z. Wang, G. A. Michaud, Z. Cheng, Y. Zhang, T. R. Hinds, E. Fan, F. Cong, W. Xu, Recognition of the iso-ADP-ribose moiety in poly(ADP-ribose) by WWE domains suggests a general mechanism for poly (ADP-ribosyl)ation-dependent ubiquitination. *Genes Dev.* **26**, 235–240 (2012).
17. A. G. Allgood, D. Barrick, Mapping the Deltex-binding surface on the notch ankyrin domain using analytical ultracentrifugation. *J. Mol. Biol.* **414**, 243–259 (2011).
18. C. Liu, A. Vyas, M. A. Kassab, A. K. Singh, X. Yu, The role of poly ADP-ribosylation in the first wave of DNA damage response. *Nucleic Acids Res.* **45**, 8129–8141 (2017).
19. H. Wei, X. Yu, Functions of PARylation in DNA damage repair pathways. *Genomics Proteomics Bioinformatics* **14**, 131–139 (2016).
20. R. Gupte, Z. Liu, W. L. Kraus, PARPs and ADP-ribosylation: Recent advances linking molecular functions to biological outcomes. *Genes Dev.* **31**, 101–126 (2017).
21. S. Jungmichel, F. Rosenthal, M. Altmeyer, J. Lukas, M. O. Hottiger, M. L. Nielsen, Proteome-wide identification of poly(ADP-ribosyl)ation targets in different genotoxic stress responses. *Mol. Cell* **52**, 272–285 (2013).
22. A. Ray Chaudhuri, A. Nussenzweig, The multifaceted roles of PARP1 in DNA repair and chromatin remodelling. *Nat. Rev. Mol. Cell Biol.* **18**, 610–621 (2017).
23. G. Soria, S. E. Polo, G. Almouzni, Prime, repair, restore: The active role of chromatin in the DNA damage response. *Mol. Cell* **46**, 722–734 (2012).
24. C. A. Vivelo, R. Wat, C. Agrawal, H. Y. Tee, A. K. L. Leung, ADPriboDB: The database of ADP-ribosylated proteins. *Nucleic Acids Res.* **45**, 6254 (2017).
25. P. A. Da Rosa, Z. Wang, X. Jiang, J. N. Pruneda, F. Cong, R. E. Klevit, W. Xu, Allosteric activation of the RNF146 ubiquitin ligase by a poly(ADP-ribosyl)ation signal. *Nature* **517**, 223–226 (2015).
26. H. C. Kang, Y.-I. Lee, J.-H. Shin, S. A. Andrabi, Z. Chi, J.-P. Gagné, Y. Lee, H. S. Ko, B. D. Lee, G. G. Poirier, V. L. Dawson, T. M. Dawson, Iduna is a poly(ADP-ribose) (PAR)-dependent E3 ubiquitin ligase that regulates DNA damage. *Proc. Natl. Acad. Sci. U.S.A.* **108**, 14103–14108 (2011).

27. Y. Zhang, S. Liu, C. Mickanin, Y. Feng, O. Charlat, G. A. Michaud, M. Schirle, X. Shi, M. Hild, A. Bauer, V. E. Myer, P. M. Finan, J. A. Porter, S.-M. A. Huang, F. Cong, RNF146 is a poly(ADP-ribose)-directed E3 ligase that regulates axin degradation and Wnt signalling. *Nat. Cell Biol.* **13**, 623–629 (2011).
28. M. Tamura, J. Gu, K. Matsumoto, S. Aota, R. Parsons, K. M. Yamada, Inhibition of cell migration, spreading, and focal adhesions by tumor suppressor PTEN. *Science* **280**, 1614–1617 (1998).
29. H. Dou, L. Buetow, G. J. Sibbet, K. Cameron, D. T. Huang, BIRC7-E2 ubiquitin conjugate structure reveals the mechanism of ubiquitin transfer by a RING dimer. *Nat. Struct. Mol. Biol.* **19**, 876–883 (2012).
30. M. Gabrielsen, L. Buetow, M. A. Nakasone, S. F. Ahmed, G. J. Sibbet, B. O. Smith, W. Zhang, S. S. Sidhu, D. T. Huang, A general strategy for discovery of inhibitors and activators of RING and U-box E3 ligases with ubiquitin variants. *Mol. Cell* **68**, 456–470.e10 (2017).
31. H. Dou, L. Buetow, A. Hock, G. J. Sibbet, K. H. Vousden, D. T. Huang, Structural basis for autoinhibition and phosphorylation-dependent activation of c-Cbl. *Nat. Struct. Mol. Biol.* **19**, 184–192 (2012).
32. S. Volk, M. Wang, C. M. Pickart, Chemical and genetic strategies for manipulating polyubiquitin chain structure. *Methods Enzymol.* **399**, 3–20 (2005).
33. H. Dou, L. Buetow, G. J. Sibbet, K. Cameron, D. T. Huang, Essentiality of a non-RING element in priming donor ubiquitin for catalysis by a monomeric E3. *Nat. Struct. Mol. Biol.* **20**, 982–986 (2013).
34. M.-F. Langelier, J. L. Planck, K. M. Servent, J. M. Pascal, Purification of human PARP-1 and PARP-1 domains from Escherichia coli for structural and biochemical analysis. *Methods Mol. Biol.* **780**, 209–226 (2011).
35. E. Gasteiger, C. Hoogland, A. Gattiker, S. Duvaud, M. Wilkins, R. D. Appel, A. Bairoch, Protein identification and analysis tools on the ExPASy server in *The Proteomics Protocols Handbook*, (Humana Press, 2005), pp. 571–607.
36. G. Winter, xia2: An expert system for macromolecular crystallography data reduction. *J. Appl. Crystallogr.* **43**, 186–190 (2010).
37. G. Winter, D. G. Waterman, J. M. Parkhurst, A. S. Brewster, R. J. Gildea, M. Gerstel, L. Fuentes-Montero, M. Vollmar, T. Michels-Clark, I. D. Young, N. K. Sauter, G. Evans, DIALS: Implementation and evaluation of a new integration package. *Acta Crystallogr. D Struct. Biol.* **74**, 85–97 (2018).
38. P. Evans, Scaling and assessment of data quality. *Acta Crystallogr. D Biol. Crystallogr.* **62**, 72–82 (2006).
39. P. R. Evans, G. N. Murshudov, How good are my data and what is the resolution? *Acta Crystallogr. D Biol. Crystallogr.* **69**, 1204–1214 (2013).
40. A. J. McCoy, R. W. Grosse-Kunstleve, P. D. Adams, M. D. Winn, L. C. Storoni, R. J. Read, Phaser crystallographic software. *J. Appl. Crystallogr.* **40**, 658–674 (2007).
41. G. Bricogne, E. Blanc, M. Brandl, C. Flensburg, P. Keller, W. Paciorek, P. Roversi, A. Sharff, O. S. Smart, C. Vonrhein, T. O. Womack, BUSTER (Global Phasing Ltd., 2016).
42. P. D. Adams, P. V. Afonine, G. Bunkóczi, V. B. Chen, I. W. Davis, N. Echols, J. J. Headd, L.-W. Hung, G. J. Kapral, R. W. Grosse-Kunstleve, A. J. McCoy, N. W. Moriarty, R. Oeffner, R. J. Read, D. C. Richardson, J. S. Richardson, T. C. Terwilliger, P. H. Zwart, PHENIX: A comprehensive Python-based system for macromolecular structure solution. *Acta Crystallogr. D Biol. Crystallogr.* **66**, 213–221 (2010).
43. V. B. Chen, W. B. Arendall III, J. J. Headd, D. A. Keedy, R. M. Immormino, G. J. Kapral, L. W. Murray, J. S. Richardson, D. C. Richardson, MolProbity: All-atom structure validation for macromolecular crystallography. *Acta Crystallogr. D Biol. Crystallogr.* **66**, 12–21 (2010).
44. G. J. Kleywegt, Use of non-crystallographic symmetry in protein structure refinement. *Acta Crystallogr. D Biol. Crystallogr.* **52**, 842–857 (1996).
45. E. Krissinel, K. Henrick, Inference of macromolecular assemblies from crystalline state. *J. Mol. Biol.* **372**, 774–797 (2007).
46. N. A. Baker, D. Sept, S. Joseph, M. J. Holst, J. A. McCammon, Electrostatics of nanosystems: Application to microtubules and the ribosome. *Proc. Natl. Acad. Sci. U.S.A.* **98**, 10037–10041 (2001).
47. N. C. Hubner, A. W. Bird, J. Cox, B. Splettstoesser, P. Bandilla, I. Poser, A. Hyman, M. Mann, Quantitative proteomics combined with BAC TransgeneOmics reveals in vivo protein interactions. *J. Cell Biol.* **189**, 739–754 (2010).
48. J. Cox, M. Mann, MaxQuant enables high peptide identification rates, individualized p.p.b.-range mass accuracies and proteome-wide protein quantification. *Nat. Biotechnol.* **26**, 1367–1372 (2008).
49. J. Cox, N. Neuhauser, A. Michalski, R. A. Scheltema, J. V. Olsen, M. Mann, Andromeda: A peptide search engine integrated into the MaxQuant environment. *J. Proteome Res.* **10**, 1794–1805 (2011).
50. UniProt Consortium, UniProt: A worldwide hub of protein knowledge. *Nucleic Acids Res.* **47**, D506–D515 (2019).
51. S. Tyanova, T. Temu, P. Sinitcyn, A. Carlson, M. Y. Hein, T. Geiger, M. Mann, J. Cox, The Perseus computational platform for comprehensive analysis of (prote)omics data. *Nat. Methods* **13**, 731–740 (2016).
52. S. F. Ahmed, N. Das, M. Sarkar, U. Chatterjee, S. Chatterjee, M. K. Ghosh, Exosome-mediated delivery of the intrinsic C-terminus domain of PTEN protects it from proteasomal degradation and ablates tumorigenesis. *Mol. Ther.* **23**, 255–269 (2015).
53. J. Cox, M. Y. Hein, C. A. Luber, I. Paron, N. Nagaraj, M. Mann, Accurate proteome-wide label-free quantification by delayed normalization and maximal peptide ratio extraction, termed MaxLFQ. *Mol. Cell. Proteomics* **13**, 2513–2526 (2014).
54. J. D. Rudolph, J. Cox, A network module for the Perseus software for computational proteomics facilitates proteome interaction graph analysis. *J. Proteome Res.* **18**, 2052–2064 (2019).
55. P. Shannon, A. Markiel, O. Ozier, N. S. Baliga, J. T. Wang, D. Ramage, N. Amin, B. Schwikowski, T. Ideker, Cytoscape: A software environment for integrated models of biomolecular interaction networks. *Genome Res.* **13**, 2498–2504 (2003).
56. G. J. Barton, ALSCRIPT: A tool to format multiple sequence alignments. *Protein Eng.* **6**, 37–40 (1993).
57. D. Liebschner, P. V. Afonine, N. W. Moriarty, B. K. Poon, O. V. Sobolev, T. C. Terwilliger, P. D. Adams, Polder maps: Improving OMIT maps by excluding bulk solvent. *Acta Crystallogr. D Struct. Biol.* **73**, 148–157 (2017).

Acknowledgments: We thank DLS for access to beamlines I03 and I04 (proposal mx16258) that contributed to the results presented here, C. Winchester for assistance in preparing and critically reviewing this manuscript, and Core Services and Advanced Technologies at the Cancer Research UK Beatson Institute (C596/A17196), with particular thanks to Proteomics and Molecular Technologies services. **Funding:** This work was supported by Cancer Research UK (A23278 to D.T.H. and A29800 to S.Z.) and the European Research Council (ERC) under the European Union's Horizon 2020 research and innovation programme (grant agreement no. 647849 to D.T.H.). **Author contributions:** Conceptualization: S.F.A., L.B., M.G., and D.T.H.; methodology: S.F.A., L.B., M.G., and D.T.H.; investigation: S.F.A., L.B., M.G., C.C., S.L., G.J.S., and D.T.H.; writing (original draft): L.B. and S.F.A.; writing (review and editing): L.B., S.F.A., M.G., C.C., and D.T.H.; formal analysis: S.F.A., L.B., M.G., S.L., and D.T.H.; visualization: S.F.A., L.B., M.G., and D.T.H.; resources: S.Z. and D.T.H.; supervision: D.T.H.; funding acquisition: D.T.H. **Competing interests:** The authors declare that they have no competing interests. **Data and materials availability:** Coordinate and structure factors for 2RD alone and 2RD bound to ADPr have been deposited in the PDB with accession code of PDB: 6Y22 (form 1), 6Y2X (form 2) and PDB: 6Y3J, respectively. Raw MS proteomics data have been deposited to the ProteomeXchange Consortium (http://proteomecentral.proteomexchange.org) via the PRIDE partner repository with the dataset identifier PXD017807. Source data for Figs. 2A and 5B are provided in data S1 and for Fig. 2C in data S2. All raw gel images generated during this study have been deposited to Mendeley Data (http://dx.doi.org/10.17632/sxpfkty7dw.2).

Submitted 3 April 2020
Accepted 9 July 2020
Published 21 August 2020
10.1126/sciadv.abc0629

Citation: S. F. Ahmed, L. Buetow, M. Gabrielsen, S. Lilla, C. Chatrin, G. J. Sibbet, S. Zanivan, D. T. Huang, DELTEX2 C-terminal domain recognizes and recruits ADP-ribosylated proteins for ubiquitination. *Sci. Adv.* **6**, eabc0629 (2020).

Science Advances

DELTEX2 C-terminal domain recognizes and recruits ADP-ribosylated proteins for ubiquitination

Syed Feroj Ahmed, Lori Buetow, Mads Gabrielsen, Sergio Lilla, Chatrin Chatrin, Gary J. Sibbet, Sara Zanivan and Danny T. Huang

Sci Adv **6** (34), eabc0629.
DOI: 10.1126/sciadv.abc0629